CHEMISTRY OF MATERIALS
Cite This: Chem. Mater. 2018, 30, 8332−8342
Article
pubs.acs.org/cm

# Rational Design of Pore Size and Functionality in a Series of Isoreticular Zwitterionic Metal−Organic Frameworks

Darpandeep Aulakh,[†,§] Timur Islamoglu,[‡,§] Veronica F. Bagundes,[†] Juby R. Varghese,[†] Kyle Duell,[†] Monu Joy,[†] Simon J. Teat,[∥] Omar K. Farha,[‡,⊥] and Mario Wriedt*[,†]

[†]Department of Chemistry & Biomolecular Science, Clarkson University, Potsdam, New York 13699, United States of America
[‡]Department of Chemistry, Northwestern University, 2145 Sheridan Road, Evanston, Illinois 60208, United States of America
[∥]Advanced Light Source, Lawrence Berkeley National Laboratory, Berkeley, California 94720, United States of America
[⊥]Department of Chemistry, Faculty of Science, King Abdulaziz University, Jeddah 21589, Saudi Arabia

Supporting Information

**ABSTRACT:** The isoreticular expansion and functionalization of charged-polarized porosity has been systematically explored by the rational design of 11 isostructural zwitterionic metal−organic frameworks (ZW-MOFs). This extended series of general structural composition $\{[M_3F(L1)_3(L2)_{1.5}]\cdot guests\}_n$ was prepared by employing the solvothermal reaction of Co and Ni tetrafluoroborates with a binary ligand system composed of zwitterionic pyridinium derivatives and traditional functionalized ditopic carboxylate auxiliary ligands (HL1·Cl = 1-(4-carboxyphenyl)-4,4′-bipyridinium chloride, Hcpb·Cl; or 1-(4-carboxyphenyl-3-hydroxyphenyl)-4,4′-bipyridinium chloride, Hchpb·Cl; and $H_2L2$ = benzene-1,4-dicarboxylic acid, $H_2$bdc; 2-aminobenzene-1,4-dicarboxylic acid, $H_2$abdc; 2,5-dihydroxy-1,4-benzenedicarboxylic acid, $H_2$dhbdc; biphenyl-4,4′-dicarboxylic acid, $H_2$bpdc; or stilbene-4,4′-dicarboxylic acid, $H_2$sdc). Single-crystal structure analyses revealed cubic crystal symmetry (*I*-43*m*, *a* = 31−36 Å) with a 3D pore system of significant void space (73−81%). The pore system features three types of pores being systematically tunable in size ranging from 17.4 to 18.8 Å (pore I), 8.2 to 12.8 Å (pore II), and 4.8 to 10.4 Å (pore III) by the choice of auxiliary ligands. All members of this series have noninterpenetrating structures and exhibit robust architectures, as evidenced by their permanent porosity and high thermal stability (up to 300 °C). The structural integrity and specific surface areas could be systematically optimized using supercritical $CO_2$ exchange methods for framework activation resulting in BET surface areas ranging from 1250 to 2250 $m^2/g$. Most interestingly, as a structural landmark, we found the pore surfaces lined with charge gradients employed by the pyridinium ligands. This key feature results in significant adsorption of carbon dioxide and methane which is attributed to polarization effects. With this contribution we pioneer the reticulation of pyridinium building blocks into extended zwitterionic networks in which specific properties can be targeted.

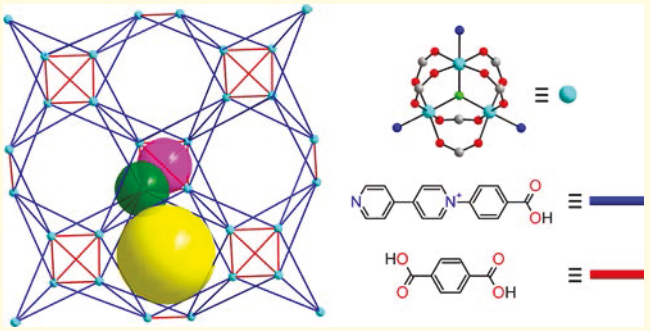

## INTRODUCTION

With a high degree of structural, chemical, and functional diversity, porous metal−organic frameworks (MOFs) have attracted considerable attention in recent years because of the potential they present in a myriad of applications such as chemical separation,[1−5] gas storage,[6,7] sensing,[8] data storage,[9−11] and catalysis[12,13] with a focus on $CO_2/N_2$ separation in our laboratory.[14−17] MOFs are extended crystalline structures composed of metal clusters or ions connected by multitopic organic ligands to build one-, two-, or three-dimensional infinite networks with fascinating structures and properties such as high surface area and high pore volume, defined pore size distribution, and good thermostability. In addition, the high degree of variability in both organic and inorganic components allows for selective tailoring of framework structures, pore environment, and functionalities.[18,19]

In contrast to current trends in the design of selective small molecule sorbents, we emphasize small molecule interactions with incorporated zwitterionic (ZW) moieties of the framework. Zwitterions are classified as molecules bearing both permanent cationic and permanent anionic functionalities which develop an electric field gradient on their molecular surface due to the well-separated intramolecular charges.[20] Their incorporation in MOFs can thus create charged organic surfaces (COSs) within the pore environment, leading to polarization effects on guest molecules, which in turn can be utilized to separate small gases based on their polarizability. For example, $CO_2$ has a significant quadrupole moment and

Received: September 12, 2018
Revised: October 24, 2018
Published: October 25, 2018






DOI: 10.1021/acs.chemmater.8b03885
Chem. Mater. 2018, 30, 8332−8342

**Scheme 1. Structural Formulas of Reported Monosubstituted Viologen-Based Ligands**[a]

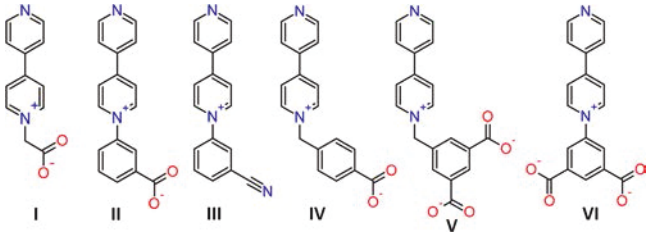


[a]Ligands **I**, **II**, **III**, and **IV** are of neutral nature, whereas **V** and **VI** carry one negative charge.[29]

polarizability[21] which enables its polarization in an electric field, thus providing the potential to form additional electrostatic interactions within the framework resulting in enhanced adsorption enthalpies.[14] In this context, most of the work has been focused on new materials originating from 1,1′-disubstituted-4,4′-bipyridinium-based ligands (viologens) exhibiting interesting photochromic behavior.[22−30] Recently, we developed an innovative design strategy to access ZW-MOFs from anionic viologen derivates. In this process, additional counterions are not required for charge compensation of a charged-balanced neutral ZW-MOF.[31] Also, we performed systematic investigations on their synthesis and derivatization.[32] The methylene groups linking pyridinium and carboxy−phenyl units in these derivates impart structural flexibility into the ligands which results in dynamic and flexible frameworks that are known to exhibit interesting adsorption, luminescent, magnetic, and photochromic behaviors as a function of host−guest interactions triggered by diverse physical and chemical stimuli.[29,30] However, since high framework stability is imperative for many practical applications, the quest for metal−organic materials with rigid frameworks has simultaneously been a subject of intense research. With this in mind, we initially synthesized two isostructural microporous MOFs with a general composition of $\{[M_3F(cpb)_3(bdc)_{1.5}]\cdot guest\}_n$ with M = Ni (**1-Ni**) and Co (**1-Co**) by the rational design of the rigid and neutral monosubstituted 4,4′-bipyridinium derivate, 1-(4-carboxyphenyl)-4,4′-bipyridinium chloride (Hcpb·Cl), and its self-assembly with metal(II) tetrafluoroborates and the auxiliary ligand 1,4-benzenedicarboxylic acid ($H_2$bdc) in DMF/EtOH mixture under solvothermal conditions. Analysis of the resulting framework topology implied potential pore size design with distinct functionalities through isoreticulation by systematic variations of the binary ligand system (HL1·Cl and $H_2$L2). Auxiliary ligands ($H_2$L2) of ditopic nature selected for this isoreticulation study include 2-aminobenzene-1,4-dicarboxylic acid ($H_2$abdc, **2**), 2,5-dihydroxybenzene-1,4-dicarboxylic acid ($H_2$dhbdc, **3**), biphenyl-4,4′-dicarboxylic acid ($H_2$bpdc, **4**), and stilbene-4,4′-dicarboxylic acid ($H_2$sdc, **5**), which resulted in seven additional isostructural materials of composition $\{[M_3F(cpb)_3(L2)_{1.5}]\cdot guest\}_n$ (**2−5-M**). Also, the ZW ligand was exchanged with 1-(4-carboxyphenyl-3-hydroxyphenyl)-4,4′-bipyridinium chloride (Hchpb·Cl) in order to extend the general feasibility of this isoreticulation approach, which resulted in two representative examples of composition $\{[M_3F(chpb)_3(bdc)_{1.5}]\cdot guests\}_n$ with M = Ni (**1′-Ni**) and Co (**1′-Co**).

Monosubstituted viologen derivates are not well explored, and to the best of our knowledge, only two studies have been reported with the ZW ligand Hcpb·Cl.[33,34] While Bezverkhyy et al. reported a series of MOFs which exhibited interesting eye-detectable thermo- and photochromic behavior, such as regular discoloration of crystals from "edge" to "core" upon $O_2$ exposure,[33] Kitagawa et al. showed that the ligand's pyridinium cationic surface participates in the strong adsorption of methanol.[34] Other explored monosubstituted viologen-based ligands are shown in Scheme 1; however, no study can be found reporting on the systematic isoreticulation and functionalization of their respective MOFs.

With this fundamental study we attempt to close this gap by presenting the synthesis, structures, and physical properties of an isoreticular series of 11 crystalline microporous MOF materials (**1−5-M** and **1′-M**). Isoreticulation enables the rational design of distinct isolated cages coexisting with interconnected 3D pore space while showing pyridinium-based charged pore linings as structural key features (Figure 1). These unique pore environments were systematically explored for their fundamental structure−property relationships of small molecule adsorption ($N_2$, $CO_2$, and $CH_4$).

## EXPERIMENTAL SECTION

**General Information.** Commercially available reagents were used as received without further purification. Viologen-based ligands Hcpb·Cl and Hchpb·Cl were synthesized using a modified literature procedure[33] (Scheme S1).

**Synthesis of Ligands 1-(4-Carboxyphenyl)-4,4′-bipyridinium Chloride (Hcpb·Cl) and 1-(4-Carboxyphenyl-3-hydroxyphenyl)-4,4′-bipyridinium Chloride (Hchpb·Cl).** A solution of 4,4′-bipyridine (3.5 g, 22.5 mmol) and 2,4-dinitrochlorobenzene (3.0 g, 15 mmol) was dissolved in 25 mL of acetone and refluxed for 13 h at 56 °C. After the mixture was cooled to room temperature, the resulting precipitates were filtered off, washed several times with dichloromethane, and dried in vacuum to give 1-(2,4-dinitrophenyl)-4,4′-bipyridinium chloride as a gray powder (3.57 g, yield 74%, Scheme S1). $^1$H NMR (400 MHz, $D_2O$): $\delta$ = 9.46 (*d*, 1H); 9.30 (*d*, 2H); 9.01 (*d*, 1H); 8.89 (*d*, 2H); 8.74 (*d*, 2H), 8.32 (*d*, 1H); 8.08 (*d*, 2H) (Figure S1). IR (KBr pellet, cm$^{-1}$): $\tilde{\nu}$ = 3505 (w), 3105 (s), 2987 (s), 1636 (s), 1613 (s), 1535 (s), 1482 (s), 1452 (m), 1410 (s), 1346 (m), 1278 (s), 1260 (m), 1239 (m), 1223 (m), 1075 (m), 1011 (s), 992 (m), 919 (s), 848 (s), 838 (w), 791 (s) (Figure S13).

To a suspension of 1-(2,4-dinitrophenyl)-4,4′-bipyridinium chloride (0.65 g, 2.0 mmol) and 2.5 mmol of triethylamine dissolved in 80% ethanol (50 mL), 4-aminobenzoic acid (0.41 g, 3.0 mmol) was added. The reaction mixture was stirred for 24 h at 90 °C. The resulting precipitates were filtered off, recrystallized from ethanol, and dried in vacuum producing Hcpb·Cl as a beige powder (0.48 g, yield 89%, Scheme S1). $^1$H NMR (400 MHz, $D_2O$): $\delta$ = 9.51 (*d*, 2H); 8.90 (*d*, 2H); 8.78 (*d*, 2H); 8.12 (*d*, 2H); 8.09 (*d*, 2H); 7.80 (*d*, 2H) (Figure S2). IR data (KBr, cm$^{-1}$): $\tilde{\nu}$ = 3330 (w), 3166 (w), 2503 (w), 1909 (w), 1678 (s), 1636 (s), 1604 (s), 1573 (s), 1557 (s), 1536 (s), 1519 (s), 1482 (s), 1452 (m), 1411 (s), 1377 (m), 1315 (m), 1274 (s), 1224 (m), 1121 (m), 1054 (m), 1013 (s), 861 (s), 814 (w), 779 (s) (Figure S13).

Hchpb·Cl was prepared similarly to Hcpb·Cl, but instead of using 4-aminobenzoic acid, 4-aminosalicylic acid (0.46 g, 3.0 mmol) was used and recrystallized from ethanol as yellow powder (0.37 g, yield 64%, Scheme S1). $^1$H NMR (400 MHz, $D_2O$): $\delta$ = 9.48 (*d*, 2H); 8.90 (*d*, 2H); 8.73 (*d*, 2H); 8.15 (*d*, 2H); 7.90 (*d*, 1H); 7.16 (*s*, 1H), 7.03 (*d*, 1H) (Figure S3). IR data (KBr, cm$^{-1}$): $\tilde{\nu}$ = 3411 (w), 3123 (w), 3069 (w), 1960 (w), 1656 (s), 1612 (s), 1497 (s), 1438 (s), 1416 (s), 1383 (s), 1282 (s), 1256 (s), 1212 (m), 1083 (s), 1062 (m), 917 (m), 864 (s), 822 (m) (Figure S13).

**Synthesis of MOFs $\{[M_3F(cpb)_3(bdc)_{1.5}]\cdot guests\}_n$ with M = Ni (1-Ni) and Co (1-Co).** Polycrystalline bulk material of **1-Ni** was prepared by the reaction of $Ni(BF_4)_2\cdot 6H_2O$ (34.0 mg, 0.1 mmol), Hcpb·Cl (31.1 mg, 0.1 mmol), and $H_2$bdc (8.3 mg, 0.05 mmol) in 2 mL of a 1:1 DMF/EtOH solvent mixture. This mixture was stirred in


DOI: 10.1021/acs.chemmater.8b03885
Chem. Mater. 2018, 30, 8332−8342

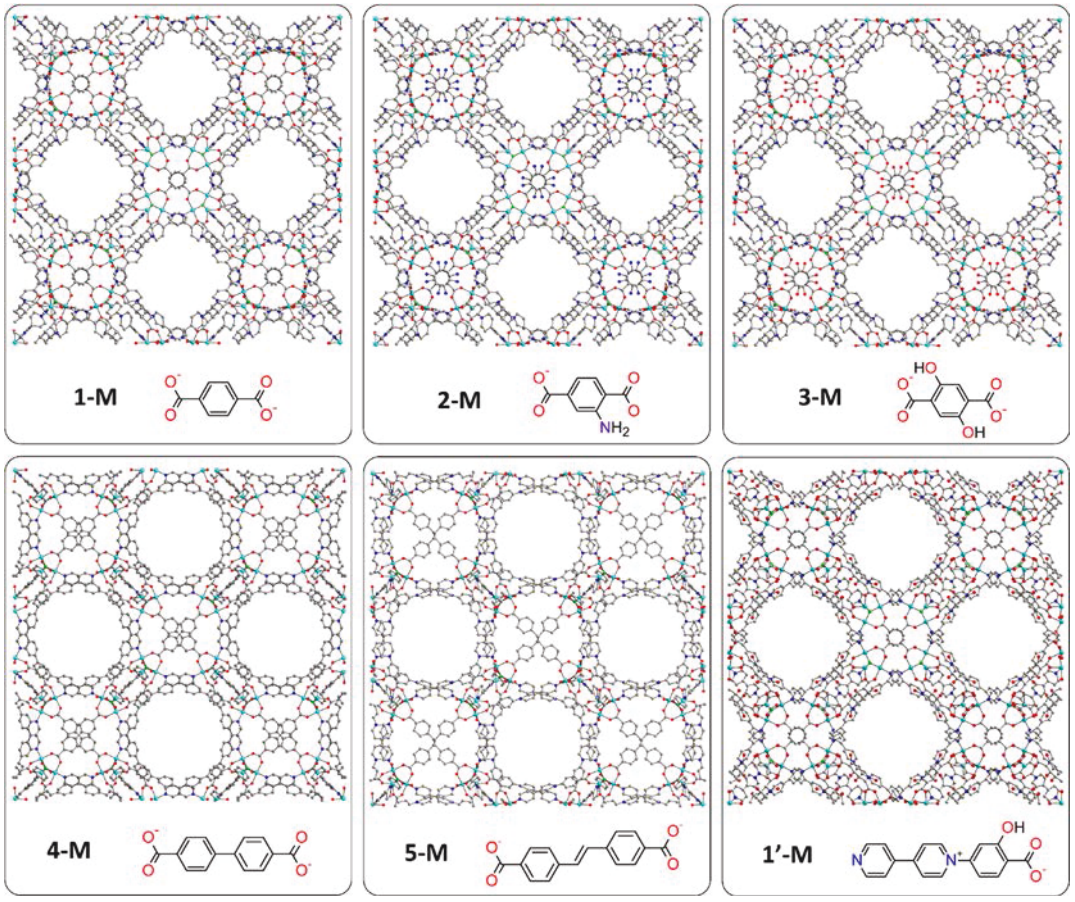


**Figure 1.** Schematic representation of functionalization and isoreticulation in a series of zwitterionic MOFs of composition $[M_3F(L1)_3(L2)_{1.5}]_n$. MOFs **1**−**5-M** are shown with Lewis structures of their respective auxiliary ligands (L2) and **1′-M** with its respective zwitterionic ligand (L1). Color code: Co/Ni, turquoise; F, green; O, red; C, gray.

a closed snap vial at 85 °C for 4 days, and the resultant green precipitates were filtered, washed with EtOH and $Et_2O$, and dried in air (yield 31 mg, 55% based on Hcpb·Cl). Pink bulk material of **1-Co** was prepared in a similar fashion as **1-Ni** using $Co(BF_4)_2{\cdot}6H_2O$ (34.0 mg, 0.1 mmol) instead of $Ni(BF_4)_2{\cdot}6H_2O$ (yield 28 mg, 52% based on Hcpb·Cl). The purity of bulk materials was confirmed by powder X-ray diffraction (PXRD) (Figure S15). Green cube-shaped crystals of **1-Ni** for single-crystal X-ray diffraction (SCXRD) studies were isolated from the reaction of a mixture containing $Ni(BF_4)_2{\cdot}6H_2O$ (34.0 mg, 0.1 mmol), Hcpb·Cl (31.1 mg, 0.1 mmol), and $H_2$bdc (8.3 mg, 0.05 mmol) in 2 mL of a 1:1 DMF/EtOH solvent mixture in a closed snap vial at 85 °C without stirring for 12 h. Pink single crystals of **1-Co** were prepared in a similar fashion as **1-Ni** but using $Co(BF_4)_2{\cdot}6H_2O$ (34.0 mg, 0.1 mmol) instead of $Ni(BF_4)_2{\cdot}6H_2O$. Complementing NMR (Figures S4 and S5), TGA (Figure S20), and CHNF analyses resulted in compositions of $\{[Ni_3F(cpb)_3(bdc)_{1.5}]\cdot(H_2bdc)\cdot(BF_4)\cdot3(NH_4)\cdot4(OH)\cdot DMF\cdot9H_2O\}_n$ for **1-Ni** and $\{[Co_3F(cpb)_3(bdc)_{1.5}]\cdot(H_2bdc)\cdot(BF_4)\cdot5(NH_4)\cdot6(OH)\cdot DMF\cdot3H_2O\}_n$ for **1-Co**. Anal. Calcd for **1-Ni**, $Ni_3BF_5N_{10}O_{30}C_{74}H_{89}$ (1880.43): C, 47.27; H, 4.77; N, 7.45; F, 5.05. Found: C, 47.84; H, 4.43; N, 7.60; F, 5.35. Anal. Calcd for **1-Co**, $Co_3BF_5N_{12}O_{26}C_{74}H_{87}$ (1843.15): C, 48.22; H, 4.76; N, 9.12; F, 5.15. Found: C, 48.67; H, 4.59; N, 9.00; F, 5.43. IR (KBr pellet, $cm^{-1}$) for **1-Ni**: $\tilde{\nu}$ = 3424 (w), 3113 (w), 3062 (w), 2666 (w), 1654 (m), 1636 (s), 1536 (s), 1491 (s), 1451 (s), 1389 (w), 1257 (s), 1083 (s), 857 (s), 824 (m). IR (KBr pellet, $cm^{-1}$) for **1-Co**: $\tilde{\nu}$ = 3425 (w), 2928 (w), 1658 (s), 1606 (s), 1535 (m), 1491 (s), 1390 (w), 1255 (s), 1096 (s), 1061 (s), 862 (m), 822 (m), 783 (m) (Figure S14).

**Synthesis of MOFs $\{[M_3F(cpb)_3(abdc)_{1.5}]\cdot guests\}_n$ with M = Ni (2-Ni) and Co (2-Co).** Polycrystalline bulk materials and single crystals were prepared in a similar fashion as **1-Ni** and **1-Co** but using $H_2$abdc (18.1 mg, 0.1 mmol) instead of $H_2$bdc (yield for **2-Ni**; 46 mg, 72%, for **2-Co**; 42 mg, 80%, both based on Hcpb·Cl). The purity of bulk materials was confirmed by PXRD (Figure S16). Complementing NMR (Figures S6 and S7), TGA (Figure S20), and CHNF analyses resulted in the composition of $\{[Ni_3F(cpb)_3(abdc)_{1.5}]\cdot(H_2abdc)\cdot3.5(BF_4)\cdot1.5(NH_4)\cdot DMF\cdot14H_2O\}_n$ for **2-Ni** and $\{[Co_3F(cpb)_3(abdc)_{1.5}]\cdot(H_2abdc)\cdot(BF_4)\cdot2(NH_4)\cdot3(OH)\cdot6H_2O\}_n$ for **2-Co**. Anal. Calcd for **2-Ni**, $Ni_3B_{3.5}F_{15}N_{11}O_{31}C_{74}H_{92.5}$ (2130.97): C, 41.71; H, 4.38; N, 7.23; F, 13.37. Found: C, 41.39; H, 3.86; N, 7.34; F, 13.01. Anal. Calcd for **2-Co**, $Co_3BF_5N_{10.5}O_{25}C_{71}H_{73.5}$ (1756.49): C, 48.55; H, 4.22; N, 8.37; F, 5.41. Found: C, 48.46; H, 4.20; N, 8.96; F, 6.04. IR (KBr pellet, $cm^{-1}$) for **2-Ni**: $\tilde{\nu}$ = 3439 (w), 3064 (m), 2930 (m), 1656 (s), 1606 (s), 1537 (s), 1394 (w), 1257 (s), 1219 (w), 1062 (w), 860 (s), 783 (s), 702 (m). IR (KBr pellet, $cm^{-1}$) for **2-Co**: $\tilde{\nu}$ = 3431 (w), 3061 (m), 1708 (m), 1636 (s), 1606 (s), 1536 (s), 1390 (w), 1219 (s), 1178 (w), 1058 (s), 820 (s), 784 (s), 701 (m) (Figure S14).

**Synthesis of MOF $\{[Co_3F(cpb)_3(dhbdc)_{1.5}]\cdot guests\}_n$ (3-Co).** Single crystals of SCXRD quality were prepared in a similar fashion as **1-Co** but using $H_2$dhbdc (19.8 mg, 0.1 mmol) instead of $H_2$bdc. Preparations of phase-pure bulk material were not successful; crystals were obtained in a heterogeneous mixture of unknown byproducts which could not be separated.

**Synthesis of MOFs $\{[M_3F(cpb)_3(bpdc)_{1.5}]\cdot guests\}_n$ with M = Ni (4-Ni) and Co (4-Co).** Polycrystalline bulk materials and single crystals were prepared in a similar fashion as **1-Ni** and **1-Co** but using $H_2$bpdc (24.2 mg, 0.1 mmol) instead of $H_2$bdc (yield for **4-Ni**; 43 mg, 80%, for **4-Co**; 41 mg, 78%, both based on Hcpb·Cl). The purity of bulk materials was confirmed by PXRD (Figure S17). Complementing NMR (Figures S8 and S9), TGA (Figure S20), and CHNF analyses resulted in the composition of $\{[Ni_3F(cpb)_3(bpdc)_{1.5}]\cdot$


DOI: 10.1021/acs.chemmater.8b03885
Chem. Mater. 2018, 30, 8332−8342

$(BF_4)\cdot(NH_4)\cdot 2(OH)\cdot DMF\cdot 11H_2O\}_n$ for **4-Ni** and $\{[Co_3F(cpb)_3(bpdc)_{1.5}]\cdot(BF_4)\cdot(NH_4)\cdot 2(OH)\cdot DMF\cdot 8H_2O\}_n$ for **4-Co**. Anal. Calcd for **4-Ni**, $Ni_3BF_5N_8O_{26}C_{75}H_{83}$ (1794.37): C, 50.2; H, 4.66; N, 6.24; F, 5.29. Found: C, 50.23; H, 4.27; N, 6.40; F, 5.95. Anal. Calcd for **4-Co**, $Co_3BF_5N_8O_{23}C_{75}H_{77}$ (1741.05): C, 51.74; H, 4.46; N, 6.44; F, 5.46. Found: C, 51.27; H, 4.25; N, 6.95; F, 6.41. IR (KBr pellet, $cm^{-1}$) for **4-Ni**: $\tilde{\nu}$ = 3420 (w), 3301 (w), 3123 (w), 3123 (w), 2512 (w), 1942 (s), 1637 (s), 1543 (m), 1490 (s), 1414 (w), 1401 (s), 1325 (s), 1218 (s), 1175 (s), 1083 (s), 956 (s), 862 (s), 783 (m). IR (KBr pellet, $cm^{-1}$) for **4-Co**: $\tilde{\nu}$ = 3418 (w), 3304 (m), 3122 (w), 2931 (w), 1658 (s), 1589 (s), 1541 (m), 1490(s), 1390 (w), 1303 (s), 1256 (s), 1083 (s), 824 (m), 758 (m) (Figure S14).

**Synthesis of MOFs $\{[M_3F(cpb)_3(sdc)_{1.5}]\cdot guests\}_n$ with M = Ni (5-Ni) and Co (5-Co).** Polycrystalline bulk materials of **5-M** and single crystals of **5-Ni** only were prepared in a similar fashion as **1-Ni** and **1-Co** but using $H_2sdc$ (26.8 mg, 0.1 mmol) instead of $H_2bdc$ (yield for **5-Ni**; 22 mg, 42 %, for **5-Co**; 19 mg, 35%, both based on Hcpb·Cl). Single-crystal growth of SCXRD quality for **5-Co** was not successful. The purity of bulk materials was confirmed by PXRD (Figure S18). Complementing NMR (Figures S10 and S11), TGA (Figure S20), and CHNF analyses resulted in the composition of $\{[Ni_3F(cpb)_3(sdc)_{1.5}]\cdot(BF_4)\cdot 2(NH_4)\cdot 3(OH)\cdot DMF\cdot 8H_2O\}_n$ for **5-Ni** and $\{[Co_3F(cpb)_3(sdc)_{1.5}]\cdot 1.5(BF_4)\cdot 1.5(NH_4)\cdot 2(OH)\cdot DMF\cdot 8H_2O\}_n$ for **5-Co**. Anal. Calcd for **5-Ni**, $Ni_3BF_5N_{9.2}O_{24}C_{78}H_{85}$ (1814.43): C, 51.63; H, 4.72; N, 6.95; F, 5.24. Found: C, 51.32; H, 4.57; N, 7.36; F, 5.91. Anal. Calcd for **5-Co**, $Co_3B_{1.5}F_7N_{8.5}O_{23}C_{78}H_{82}$ (1832.53): C, 51.12; H, 4.51; N, 6.5; F, 7.26. Found: C, 51.52; H, 4.22; N, 6.56; F, 6.95. IR (KBr pellet, $cm^{-1}$) for **5-Ni**: $\tilde{\nu}$ = 3439 (w), 3122 (m), 3067 (w), 2933 (w), 1657 (s), 1639 (s), 1605 (m), 1537 (s), 1490 (s), 1389 (w), 1256 (s), 1062 (s), 822 (s), 784 (m). IR (KBr pellet, $cm^{-1}$) for **5-Co**: $\tilde{\nu}$ = 3427 (w), 3117 (m), 3063 (w), 2927 (w), 1659 (s), 1605 (s), 1491 (m), 1389 (w), 1256 (s), 1083 (s), 1062 (m), 823 (s), 785 (s), 704 (m) (Figure S14).

**Synthesis of MOF $\{[Ni_3F(chpb)_3(bdc)_{1.5}]\cdot guests\}_n$ with M = Ni (1′-Ni) and Co (1′-Co).** Polycrystalline bulk material for **1′-Ni** and single crystals for **1′-M** were prepared in a similar fashion as **1-Ni** and **1-Co** but using Hchpb·Cl (32.7 mg, 0.1 mmol) instead of Hcpb·Cl (yield 46 mg, 67% based on Hchpb·Cl). Preparation of phase-pure bulk material of **1′-Co** was not successful; crystals were obtained in a heterogeneous mixture of unknown byproducts which could not be separated. The purity of bulk material for **1′-Ni** was confirmed by PXRD (Figure S19). Complementing NMR (Figure S12) and CHNF analyses resulted in the composition of $\{[Ni_3F(chpb)_3(bdc)_{1.5}]\cdot(H_2bdc)\cdot 3(BF_4)\cdot 2(NH_4)\cdot(OH)\cdot DMF\cdot 9H_2O\}_n$ for **1′-Ni**. Anal. Calcd for $Ni_3B_3F_{13}N_9O_{30}C_{74}H_{82}$ (2032.97): C, 43.72; H, 4.07; N, 6.20; F, 12.15. Found: C, 43.67; H, 3.48; N, 6.21; F, 11.63. IR (KBr pellet, $cm^{-1}$): $\tilde{\nu}$ = 3429(w), 3103 (w), 3072 (w), 2698 (w), 1684 (m), 1612 (s), 1542 (s), 1467 (s), 1451 (s), 1378 (w), 1243 (s), 1056 (s), 834 (s), 819 (m) (Figure S14).

**Single-Crystal Structure Analysis.** Single crystals were selected and mounted on MiTeGen loops in Paratone oil. Crystal data of compounds **1-Co**, **3-Co**, **5-Ni**, and **1′-Ni/Co** were collected on a Bruker Kappa Apex II X-ray diffractometer outfitted with a Mo X-ray source (sealed tube, $\lambda$ = 0.71073 Å) and an APEX II CCD detector equipped with an Oxford Cryosystems Desktop Cooler low-temperature device. The APEX3 software suite was used for data collection, cell refinement, and reduction.[35] Absorption corrections were applied using SADABS.[36] Space group assignments were determined by examination of systematic absences, *E*-statistics, and successive refinement of the structures. Structure solutions were performed with intrinsic phasing using SHELXT-2014 and refined by least-squares refinement against $|F|^2$ followed by difference Fourier synthesis using SHELXL-2014.[37−39] If not stated differently, non-hydrogen atoms were refined with anisotropic displacement parameters. Aromatic C−H atoms were positioned with idealized geometry and refined with fixed isotropic displacement parameters $[U_{eq}(H) = -1.2U_{eq}(C)]$ using a riding model with $d_{C-H}$ = 0.95 Å. Crystal data of compounds **1-Ni**, **2-Ni/Co**, and **4-Ni/Co** were collected on a Bruker D8 diffractometer equipped with a PHOTON100 CMOS detector and Oxford Cryosystems Cryostream 800 plus on Beamline 11.3.1 of the Advanced Light Source at Lawrence Berkeley National Lab using silicon (111) monochromated synchrotron radiation ($\lambda$ = 0.7749 Å). Dispersion corrections appropriate for this wavelength were calculated using the Brennan method in XDISP[40] within WinGX.[41] Structure solutions and refinements were performed similar as described above.

CCDC 1863492−1863501 contain the supplementary crystallographic data for this paper. These data can be obtained free of charge from the Cambridge Crystallographic Data Centre via www.ccdc.cam.ac.uk. Selected crystal data and details on structure determinations are listed in Table 1.

**Powder X-ray Diffraction (PXRD).** PXRD data for compounds **1-M**, **2-M**, and **4-M** were recorded on the 17BM beamline at the Advanced Photon Source, Argonne National Laboratory (Argonne, IL, USA). The incident X-ray wavelength was 0.72768 Å. Data were collected using a PerkinElmer flat panel area detector (XRD 1621 CN3-EHS) over the angular range 1−20° 2-Theta. PXRD data for **5-M** and **1′-Ni** were collected on a Bruker D2 Phaser diffractometer equipped with a Cu sealed tube ($\lambda$ = 1.54178 Å). Powder samples were dispersed on low-background discs for analyses. Simulation of the PXRD data was performed by using single-crystal data and the powder pattern module of the mercury CSD software package.[42]

**Thermogravimetric Analysis (TGA).** TG data was collected with a TGA Q50 from TA Instruments. All measurements were performed using platinum crucibles in a dynamic nitrogen atmosphere (50 mL/min) and a heating rate of 3 °C·min$^{-1}$. The instrument was corrected for buoyancy and current effects and was calibrated using standard reference materials.

**Adsorption Analysis.** Supercritical $CO_2$ drying was performed using a TousimisTM Samdri PVT-30 critical point dryer (Tousimis, Rockville, MD, USA). The as-synthesized samples were activated by soaking in ethanol for 2 days, during which time ethanol was replenished three times. The supercritical $CO_2$ was bled off at a rate of 0.5 mL/min until the chamber reached ambient pressure (typically overnight). The chamber was opened, and the sample was quickly capped and transferred into an argon-filled glovebox where it was transferred to a preweighed sample tube. The evacuated analysis tubes containing the activated samples were then carefully transferred to an electronic balance and weighed to determine the sample mass. The tubes were then transferred to the analysis port of the gas adsorption instrument. The samples were kept under vacuum at room temperature for 2 h prior to $N_2$ adsorption isotherm collection. $N_2$ isotherms were measured by a volumetric gas analyzer using a Micromeritics Tristar II 3020 (Micromeritics, Norcross, GA); $CO_2$ and $CH_4$ isotherms were collected on ASAP2020. For all isotherms, warm and cold free space correction measurements were performed using ultrahigh-purity He gas (UHP grade 5.0, 99.999% purity). All gases used are UHP grade (99.999% purity). $N_2$ isotherms at 77 K were measured in liquid nitrogen; isotherms at 273, 288, and 298 K were measured using temperature circulating baths. All temperatures and fill levels were monitored periodically throughout the measurement.

**Elemental Analysis.** Elemental data (C, H, N and F) was obtained from Atlantic Microlab, Inc.

**Spectroscopy.** FT-IR data were recorded on a Nicolet iS10 from Thermo Scientific. $^1$H NMR data were recorded on Avance DMX-400 from Bruker.

## RESULTS AND DISCUSSION

**Crystal Structures and Synthetic Strategies.** The preparation of materials was optimized into a consistent synthesis scheme: Ni or Co tetrafluoroborates reacted under solvothermal conditions with a binary ligand mixture composed of a pyridinium-carboxyl ZW ligand (HL1·Cl = Hcpb·Cl or Hchpb·Cl) and a traditional carboxyl auxiliary ligand ($H_2L2$ = $H_2bdc$, $H_2abdc$, $H_2dhbdc$, $H_2bpdc$, or $H_2sdc$). Employing this scheme, 11 isoreticular materials (**1−2-Ni**, **4−5-Ni**, **1−5-Co**, **1′-Ni**, and **1′-Co**) could be crystallized.


DOI: 10.1021/acs.chemmater.8b03885
Chem. Mater. 2018, 30, 8332−8342

**Table 1. Selected Crystal Data and Details on Structure Determinations from SCXRD Analysis**

| | 1-Ni | 1-Co | 2-Ni | 2-Co | 3-Co |
|---|---|---|---|---|---|
| formula[a] | $Ni_3BF_5N_{10}O_{30}C_{74}H_{89}$ | $Co_3BF_5N_{12}O_{26}C_{74}H_{87}$ | $Ni_3B_{3.5}F_{15}N_{11}O_{31}C_{74}H_{92.5}$ | $Co_3BF_5N_{10.5}O_{25}C_{71}H_{73.5}$ | $Co_3FN_6O_{15}C_{60}H_{12}$[b] |
| composition[c] | $[Ni_3F(cpb)_3(bdc)_{1.5}]_n$ | $[Co_3F(cpb)_3(bdc)_{1.5}]_n$ | $[Ni_3F(cpb)_3(abdc)_{1.5}]_n$ | $[Co_3F(cpb)_3(abdc)_{1.5}]_n$ | $[Co_3F(cpb)_3(dhbdc)_{1.5}]_n$ |
| MW [g·mol$^{-1}$] | 1880.43 | 1843.15 | 2130.97 | 1756.49 | 1252.55 |
| cryst syst | cubic | cubic | cubic | cubic | cubic |
| space group | *I*-43*m* | *I*-43*m* | *I*-43*m* | *I*-43*m* | *I*-43*m* |
| *a* [Å] | 32.0068(10) | 32.340(4) | 31.9734(9) | 32.2073(10) | 32.3227(11) |
| *V* [Å$^3$] | 32789(3) | 33825(11) | 32686(3) | 33409(3) | 33769(3) |
| *T* [K] | 100(2) | 170(2) | 100(2) | 100(2) | 170(2) |
| *Z* | 8 | 8 | 8 | 8 | 8 |
| $D_{calc}$ [g·cm$^{-3}$] | 0.617 | 0.501 | 0.634 | 0.620 | 0.493 |
| $\mu$ [mm$^{-1}$] | 0.475 | 0.316 | 0.478 | 0.416 | 0.317 |
| min/max transmission | 0.857/0.981 | 0.552/0.745 | 0.863/0.967 | 0.822/0.936 | 0.673/0.746 |
| $\theta_{max}$ [deg] | 28.563 | 25.025 | 28.934 | 28.567 | 24.985 |
| no. of measd reflns | 15 4167 | 32 396 | 16 1125 | 159 332 | 32 882 |
| no. of unique reflns | 5822 | 5404 | 6012 | 5929 | 5367 |
| no. of params | 180 | 210 | 188 | 188 | 176 |
| $R_{int}$ | 0.0498 | 0.1786 | 0.0430 | 0.0448 | 0.0996 |
| $R_1$ [$F_0 > 4\sigma(F_0)$] | 0.0834 | 0.0536 | 0.0843 | 0.0906 | 0.0420 |
| $wR_2$ [all data] | 0.2450 | 0.1137 | 0.2516 | 0.2686 | 0.0906 |
| GOF | 1.180 | 0.951 | 1.203 | 1.163 | 0.978 |
| $\Delta\rho_{max}/\Delta\rho_{min}$ [e·Å$^{-3}$] | 1.002/−0.655 | 0.246/−0.259 | 1.290/−0.627 | 0.840/−0.650 | 0.231/−0.215 |
| | **4-Ni** | **4-Co** | **5-Ni** | **1′-Ni** | **1′-Co** |
| formula[a] | $Ni_3BF_5N_8O_{26}C_{75}H_{83}$ | $Co_3BF_5N_8O_{23}C_{75}H_{77}$ | $Ni_3BF_5N_{9.2}O_{24}C_{78}H_{85}$ | $Ni_3B_3F_{13}N_9O_{30}C_{74}H_{82}$ | $Ni_3B_3FN_6O_{15}C_{64.2}H_{33.3}$[b] |
| composition[c] | $[Ni_3F(cpb)_3(bpdc)_{1.5}]_n$ | $[Co_3F(cpb)_3(bpdc)_{1.5}]_n$ | $[Ni_3F(cpb)_3(sdc)_{1.5}]_n$ | $[Ni_3F(chpb)_3(bdc)_{1.5}]_n$ | $[Co_3F(chpb)_3(bdc)_{1.5}]_n$ |
| MW [g·mol$^{-1}$] | 1794.37 | 1741.05 | 1814.43 | 2032.97 | 1324.46 |
| cryst syst | cubic | cubic | cubic | cubic | cubic |
| space group | *I*-43*m* | *I*-43*m* | *I*-43*m* | *I*-43*m* | *I*-43*m* |
| *a* [Å] | 34.9443(14) | 35.0946(10) | 36.3790(9) | 32.141(2) | 32.3395(6) |
| *V* [Å$^3$] | 42671(5) | 43224(4) | 48145(4) | 33204(7) | 33822(2) |
| *T* [K] | 100(2) | 100(2) | 180(2) | 170(2) | 170(2) |
| *Z* | 8 | 8 | 8 | 8 | 8 |
| $D_{calc}$ [g·cm$^{-3}$] | 0.526 | 0.520 | 0.378 | 0.515 | 0.520 |
| $\mu$ [mm$^{-1}$] | 0.368 | 0.324 | 0.251 | 0.363 | 0.318 |
| min/max transmission | 0.750/0.914 | 0.863/0.935 | 0.720/0.610 | 0.662/0.745 | 0.55/0.63 |
| $\theta_{max}$ [deg] | 31.082 | 28.964 | 25.016 | 24.990 | 24.990 |
| no. of measd reflns | 226269 | 213469 | 84980 | 29177 | 56497 |
| no. of unique reflns | 9428 | 7891 | 7624 | 5289 | 5382 |
| no. of params | 223 | 223 | 140 | 186 | 207 |
| $R_{int}$ | 0.0574 | 0.0446 | 0.1805 | 0.0938 | 0.0891 |
| $R_1$ [$F_0 > 4\sigma(F_0)$] | 0.0766 | 0.0888 | 0.0727 | 0.0508 | 0.0381 |
| $wR_2$ [all data] | 0.2364 | 0.2654 | 0.2223 | 0.1377 | 0.0995 |
| GOF | 1.157 | 1.208 | 1.044 | 1.018 | 1.036 |
| $\Delta\rho_{max}/\Delta\rho_{min}$ [e·Å$^{-3}$] | 1.329/−0.916 | 1.145/−0.527 | 0.440/−0.602 | 0.320/−0.295 | 0.239/−0.261 |

[a]Formula reflects framework composition and also molecules occupying the voids as obtained from elemental analysis. [b]Formula reflects framework from SCXRD data only, no bulk composition available. [c]Composition reflects the core framework only.

SCXRD analysis revealed a core framework composition of $[M_3F(L1)_3(L2)_{1.5}]_n$ (Figures S21−S30). Their large void spaces and severe disorder of guest molecules resulted in very weak diffraction using conventional laboratory X-ray sources. Hence, synchrotron radiation was used to obtain high-resolution data sets for **1-Ni**, **2-Ni/Co**, and **4-Ni/Co**. Compounds **1-Co**, **3-Co**, **5-Ni**, and **1′-Ni/Co** could be refined from conventional data. Identification of **5-Co** was confirmed by PXRD alone as no quality single crystals could be grown (Figure S18). The crystal structure of **1-Ni** is discussed below in detail as a representative example of the isoreticular series. **1-Ni** crystallizes in the noncentrosymmetric cubic space group *I*-43*m* with eight formula units per unit cell. The asymmetric unit consists of one $Ni^{2+}$ cation (S.O.F. 1/2, site *m*), one $F^-$ anion (S.O.F. 1/6, site 3*m*), and fractions of the ligands, 1/2 cpb and 1/4 bdc (Figure S21). The crystal structure exhibits 9-connected tricapped trigonal-prismatic metal nodes composed of corner-sharing octahedrally coordinated $Ni^{2+}$ cations (Figure 2A). The equatorial positions of these trimeric $Ni^{2+}$-centered octahedra are connected by six bidentate carboxyl groups of three L1 cpb ZW ligands and three L2 $bdc^{2-}$ auxiliary ligands. The inner-facing octahedral axial positions share one central $\mu_3$-$F^-$ anion, whereas the outer-facing axial positions feature bridging *N*-coordinated cpb ligands (Figure 2A). This structural arrangement leads to three Ni-($\mu_3$-F)-Ni angles of 120°. Interestingly, only 17 $\mu_3$-F-bridged metal trimers of composition $[M_3F(O_2CR)_3X_{1.5}]$ vs 768 oxo-bridged trimers are reported in the Cambridge Structure Database



DOI: 10.1021/acs.chemmater.8b03885
*Chem. Mater.* 2018, 30, 8332−8342

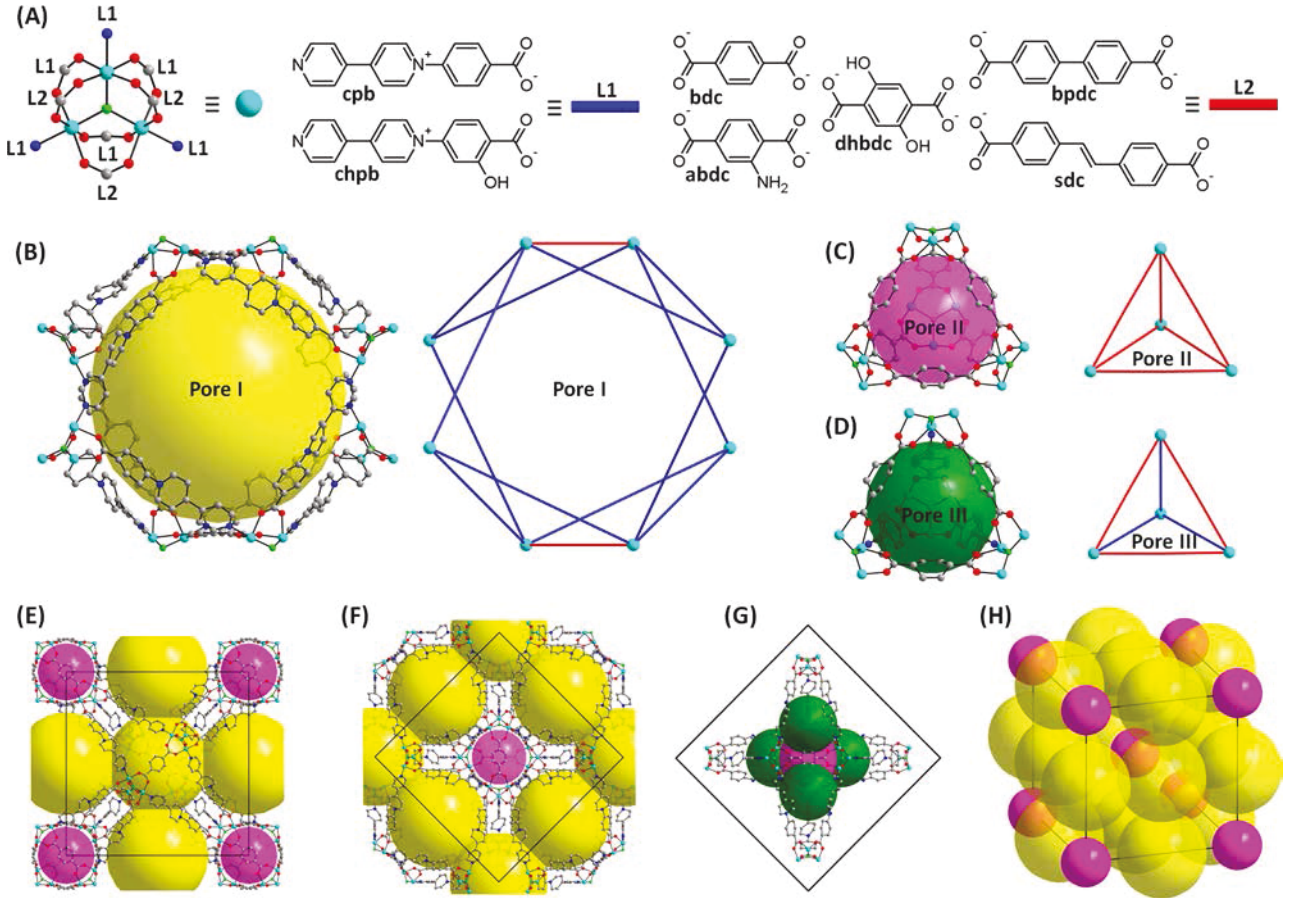


**Figure 2.** Structural features of isoreticular series: (A) 9-connected metal node of composition $M_3F(L1)_6(L2)_3$ with respective linear bridging ligands (L1 blue and L2 red). (B–D) Building blocks of **1-Ni** (L1 = cpb, L2 = bdc) as a representative example of isoreticular series. (B) Pseudo-octagonal channel-type pore of composition $(Ni_3F)_8(L1)_{12}(L2)_2$ (pore I, yellow sphere of Ø 18.8 Å). (C) Regular tetrahedral cage-type pore of composition $(Ni_3F)_4(L2)_6$ (pore II, pink sphere of Ø 8.2 Å). (D) Trigonal-pyramidal cage-type pore of composition $(Ni_3F)_4(L1)_3(L2)_3$ (pore III, green sphere of Ø 5.6 Å. (E–H) Crystal packings of **1-Ni**. (E) Pores I are each interconnected by four adjacent pores of the same type, while pores II are isolated of pores I. (F and G) Pores II are interconnected by four pores III in a tetrahedral fashion while each being surrounded by six interconnected pores I. (H) 3D arrangement of pores I and II; interconnection of pores I results in 1D channel-type pores running along the cube faces. Note that pores III have been omitted for the sake of clarity in packings E, F, and H.

(CSD, Nov 2017), with the herein presented structures being the first porous fluoro-bridged examples. The 9-connected trimeric metal nodes result in a **ncb**-type network topology.[43−47] This net features in **1-Ni** three type of pores (pores I, II and III) in a 3:1:4 ratio (Figure 2B–D). Pore I is mainly composed of L1 edges resulting in a quasi-bisdisphenoidal cage of composition $(Ni_3F)_8(L1)_{12}(L2)_2$ fitting a sphere of 18.8 Å in diameter (Figure 2B). Each pore is interconnected by four adjacent pores of the same type through large apertures (Figure 2E) resulting in a **nbo**-type three-dimensional channel system (Figure 2H) which is responsible for the largest portion of the 72% void space within the framework. The channel topology has a pseudo-octagonal nature running along the cube faces featuring cationic pyridinium sites pointing toward the inner core. Three L2 ligands of each Ni trimer bridge adjacent trimers into a regular tetrahedral cage of composition $(Ni_3F)_4(L2)_6$ fitting a sphere of 8.2 Å in diameter, denoted as pore II (Figure 3C), whereas pores I and II are not interconnected. The size of this cavity is only determined by the length of L2. Pore III is a trigonal-pyramidal cage of composition $(Ni_3F)_4(L1)_3(L2)_3$ fitting a sphere of 5.6 Å in diameter. Each pore II connects with four pores III through small apertures to form **bcu** arrays of isolated triakis tetrahedral cages (Figure 2G). Interestingly, changing the length of L2 can anisotropically modulate the size and shape of pore III. Finally, the isolated **bcu** cavities [(pore II)(pore III)$_4$] connect to the **nbo** channel through small apertures between pore III and pore I, furnishing a hierarchical channel–cavity biporous system.[45]

Modulation and precise control of MOF structures to yield topologies with high porosity is crucial for their function. Although some ZW-MOFs have been previously reported, these materials possess mostly highly dense low-porosity structures; thus, their effective modulation of porosity still remains a significant design and synthetic challenge. Herein, we report the first example of the modulation of porosity in a series of ZW-MOFs via a strategy of selective elongation of metal–organic cages. Initial structural investigations of **1-Ni** and **1-Co** set the stage to design an isoreticular series with various pore sizes, surface areas, and functionalities by replacing $bdc^{2-}$ with structurally related ditopic carboxylate linkers (Figure 3). Indeed, using each of the linkers 2-aminobenzene-1,4-dicarboxylate (**2**), 2,5-dihydroxybenzene-1,4-dicarboxylate (**3**), biphenyl-4,4′-dicarboxylate (**4**), and stilbene-4,4′-dicarboxylate (**5**) instead of $bdc^{2-}$ yielded **2-Ni/Co** through **5-Ni/Co**. Each member of this ZW-MOF series


DOI: 10.1021/acs.chemmater.8b03885
*Chem. Mater.* 2018, 30, 8332–8342

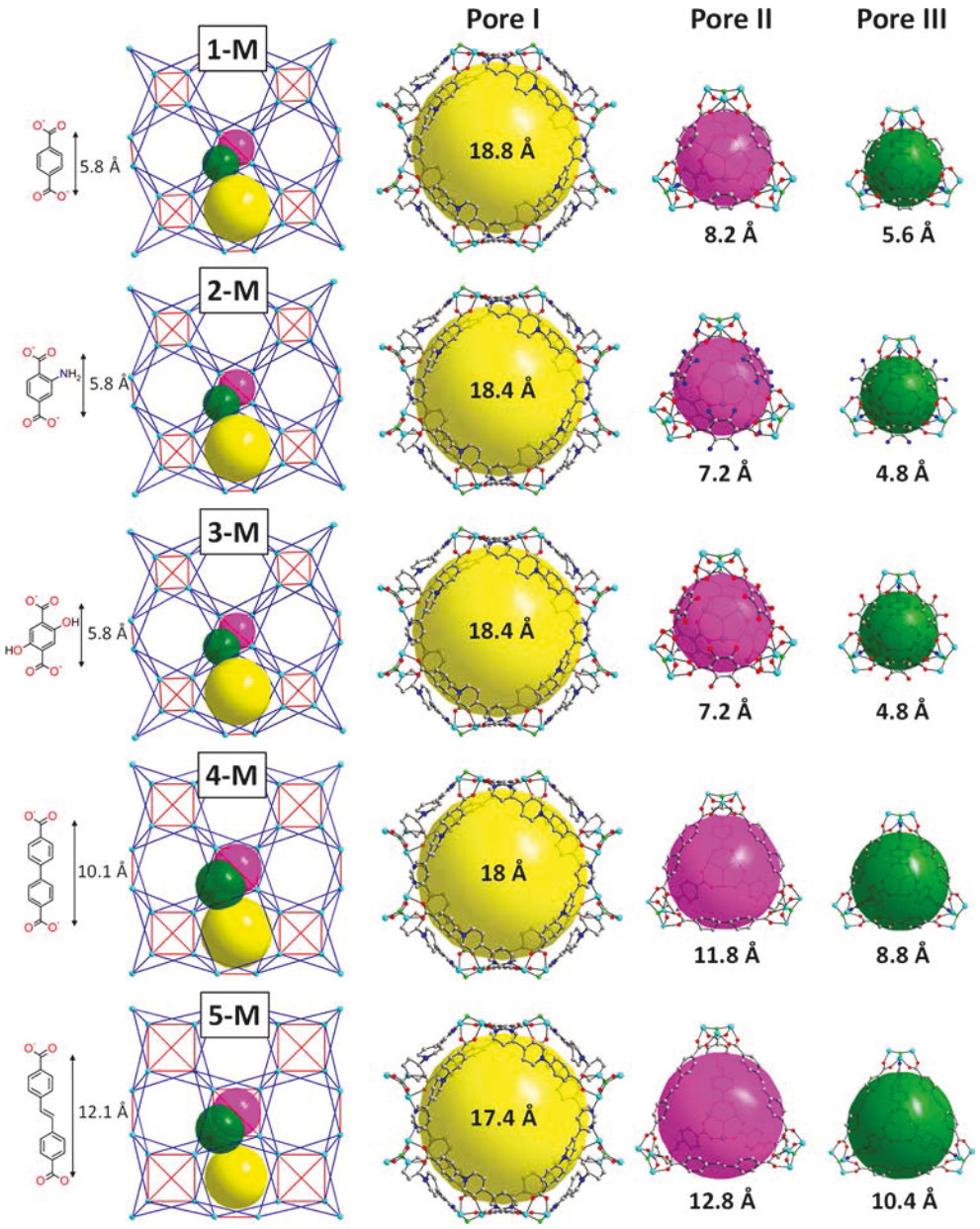


**Figure 3.** Schematic representation of crystal structures of isoreticular series **1**−**5-M** along with their respective pore structures, pore dimensions, and Lewis structures of modulating auxiliary ligands. All structures shown are composed of the ZW ligand cpb (Figure 2A).

has been isolated and was formulated subsequently by chemical microanalysis, TGA, and SCXRD studies (Table 1). In common, the crystal structures of **1**−**5-M** exhibit a 3D cubic porous network differing in the nature of functional groups decorating the pores and in the metrics of their pore structure (Figures 3 and S31). Thus, by varying the length and nature of the polyaromatic cores of the linkers L2 on going from **1-M** to **5-M**, we rationally extended the length of metal−organic cages and effectively avoided framework interpenetration. The largest spheres that can fit within these cages, taking into account the van der Waals radii of surface atoms, have diameters of 17.4−18.8 (pore I), 8.2−12.8 (pore II), and 4.8−10.4 Å (pore III). We also show that the isoreticular series **1**−**5-M** can be further expanded by changing the ZW ligand L1. Representatively, we synthesized **1′-M** under conditions identical for **1-M** by replacing cpb with chpb.

**Adsorption Properties.** While single-crystal analysis confirmed the formation of low-density (high-porosity) ZW-MOFs, maintaining the porosity upon solvent removal is very crucial for potential applications. Conventional solvent exchange routes followed by thermal activation under vacuum for MOF activation consistently resulted in framework collapse as indicated by PXRD and BET analysis. Thus, supercritical $CO_2$ exchange methods were successfully employed as mild alternative routes for framework activation.[48,49] Subsequently, selected MOFs were characterized for their specific surface areas and pore volumes as elucidated from $N_2$ isotherms collected at 77 K (Figure 4 and Table 2). **1-Ni** revealed a permanent porosity after solvent removal and BET surface area as high as 2400 $m^2\ g^{-1}$ and total pore volume of 0.929 $cm^3\ g^{-1}$. The isotherm up to a relative pressure ($p/p_0$) of 1.0 revealed a reversible type I behavior with no significant hysteresis between the sorption and the desorption traces, attributed to


DOI: 10.1021/acs.chemmater.8b03885
Chem. Mater. 2018, 30, 8332−8342

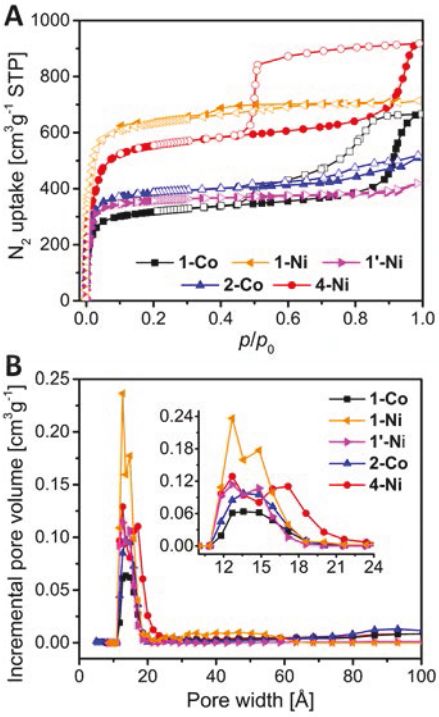


**Figure 4.** $N_2$ adsorption isotherms at 77 K (A) and corresponding pore size distribution plots (B) for MOFs **1-Co**, **1-Ni**, **1′-Ni**, **2-Co**, and **4-Ni**.

**Table 2. Selected Porosity Parameters of MOFs 1-Co, 1-Ni, 1′-Ni, 2-Co, and 4-Ni**

| MOF | surface area ($m^2\ g^{-1}$) | $N_2$ uptake ($cm^3\ g^{-1}$)[a] | PSD (Å) | pore volume ($cm^3\ g^{-1}$) |
|---|---|---|---|---|
| **1-Co** | 1250 | 407 | 13.7 | 0.462 |
| **1-Ni** | 2400 | 659 | 12.6/14.8 | 0.929 |
| **1′-Ni** | 1500 | 384 | 12.6/14.8 | 0.494 |
| **2-Co** | 1600 | 478 | 13.8 | 0.589 |
| **4-Ni** | 2250 | 705 | 12.7/16.8 | 0.816 |

[a]At 0.85 $p/p_0$ and 77 K (values 0.85−1.0 $p/p_0$ are in part affected by $N_2$ condensation)

the key features of its interconnected 3D channel pores. The sorption reaches near saturation at low relative pressures ($p/p_0$ < 0.05) and thereafter increases very slowly up to 1 atm, indicating the microporous nature of the framework. Similar type I behavior with a high $N_2$ adsorption plateau and the absence of hysteresis indicative of microporosity was exhibited by **1′-Ni** and **2-Co**. The steep increase in the $N_2$ isotherm after $p/p_0$ = 0.8 for **1-Co** and **4-Ni** can be attributed to the condensation of $N_2$ within the intercrystallite void spaces. It was found that the $N_2$ adsorption capacity decreases in the order **5-Ni** < **4-Ni** < **1-Ni** (Figures 4A and S32). This is in full agreement with the decreasing length of the pillar linkers from $sdc^{2-}$ to $bpdc^{2-}$ to $bdc^{2-}$. Surprisingly, although **1′-Ni** and **1-Co** have similar pore sizes as **1-Ni**, their $N_2$ uptake under the conditions studied was very low compared to **1-Ni**. For **2-Ni** and **5-Ni**, even the use of supercritical $CO_2$ drying did not lead to decent surface areas, possibly due to framework instability in EtOH (Figure S32 and Table S1).

The incremental pore size distribution (PSD) curves obtained from $N_2$ adsorption isotherms by using the density functional theory (DFT) method for cylindrical pores are shown in Figure 4B. Importantly, two different pore sizes were observed for **1-Ni**, **1′-Ni**, and **4-Ni** where the larger pores can be attributed to the interconnected channels (pore I) and the smaller ones to the cage-like pores II and III between the nodes. The pore sizes of the frameworks **1-Co** and **2-Co**, as calculated from $N_2$ sorption studies, are found to be ∼13.8 Å, which can be attributed to the incomplete activation of the frameworks resulting from the presence of ZW ligands in the pores as confirmed by NMR measurements (Figures S5 and S7).

Additionally, the short-term air stability was also assessed by exposing **1-Ni** to air for 3 h followed by activation at 120 °C under dynamic vacuum, confirming the retention of porosity (Figure S33).

The microporous nature and presence of charged pore linings in the studied frameworks prompted us to explore their $CO_2$ and $CH_4$ adsorption properties at noncryogenic temperatures and to calculate the corresponding binding affinities. The sorption isotherms of $CO_2$ and $CH_4$ at 273 K for the activated frameworks probed up to a relative pressure ($p/p_0$) of 1.0 at STP are reported in Figure 5A and 5B. We were pleased to discover that the maximal $CO_2$ uptake was reported for **4-Ni** (∼3 mmol $g^{-1}$ at 273 K and 1 bar), which also exhibits the highest surface area among the other MOFs studied here and double that of [Cu(ipq)]($BF_4$) (where $H_2ipq^+$ = 1-(3,5-dicarboxyphenyl)-4-(pyridin-4-yl)pyridinium) reported by Shimizu et al.[50] The $CO_2$ and $CH_4$ adsorption isotherms at 273, 288, and 298 K were employed to calculate the respective $Q_{st}$ values through the Clausius−Clapeyron equation, representing the relative magnitude of the adsorbate−adsorbent and adsorbate−adsorbate interactions (Figures 5C, 5D, and S35−S37). It is worth noting that $CO_2$ isotherms do not show steep uptake at low pressures which confirms that the $CO_2$−framework interactions are solely physisorption. Additionally, this also confirms that metals are coordinatively saturated and there are no defects (e.g., missing linkers) around the node which would result in open $Ni^{2+}/Co^{2+}$ adsorption sites and therefore strong adsorption of $CO_2$.[51] Two successive $CO_2$ isotherms on **2-Co** (which presents primary amine moiety) at 298 K were also collected without activation after the first measurement, and the reasonable overlap between two measurements confirms the regeneration of the material without applying heat (Figure S34). Physisorptive-type interactions with $CO_2$ were further confirmed by the binding affinity calculations where zero-coverage binding affinities are calculated to be around 24−32 kJ $mol^{-1}$. This is desirable as it translates into less energy input for sorbent regeneration. Logically, the binding affinity of $CO_2$ decreases with loading as the higher affinity sites are saturated. The highest $CH_4$ uptake was observed with **4-Ni**, among others, due to its high surface area. Unlike $CO_2$, binding affinities for $CH_4$ did not decrease with increased loading, suggesting that $CH_4$ shows a similar affinity to all sites within the framework.

## CONCLUSIONS

The rational design and synthesis of a series of 11 porous zwitterionic MOFs was explored via a reticular synthesis approach by employing a variety of ditopic carboxylate linkers with diverse functional groups. The novel and intrinsic value of this design approach lies in the ability to control and direct the reticulation of pyridinium building blocks into extended networks in which specific properties can be targeted. Single-crystal structure evaluations revealed that their unique three-


DOI: 10.1021/acs.chemmater.8b03885
Chem. Mater. 2018, 30, 8332−8342

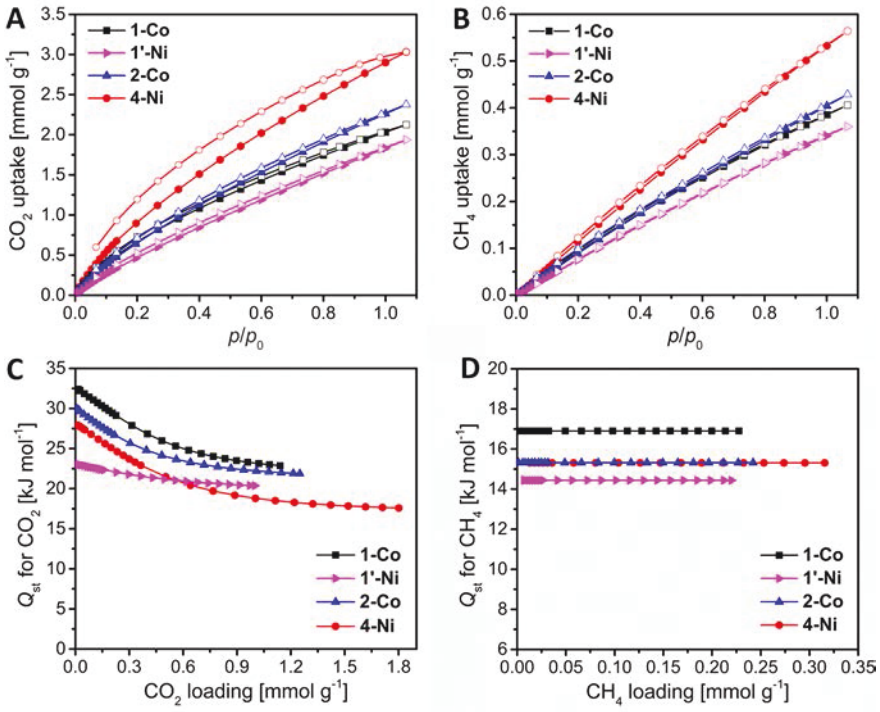


**Figure 5.** (A) $CO_2$ and (B) $CH_4$ adsorption isotherms at 273 K for **1-Co**, **1′-Ni**, **2-Co**, and **4-Ni** and the corresponding isosteric heats of (C) $CO_2$ and (D) $CH_4$ adsorption.

dimensional pore systems could be systematically tuned by varying the linker groups from 2-aminobenzene-1,4-dicarboxylate ($abdc^{2-}$) and 2,5-dihydroxybenzene-1,4-dicarboxylate ($dhbdc^{2-}$) to biphenyl-4,4′-dicarboxylate ($bpdc^{2-}$) and stilbene-4,4′-dicarboxylate ($sdc^{2-}$). In addition, supercritical $CO_2$ activation methods were employed to optimize specific surface areas and adsorption capacities. Given the unique structural attributes of the herein studied isoreticular MOF series, including their thermal stability and adsorption properties, it is expected that this work will contribute to inspire the development of new structural design strategies for the discovery of specifically underexplored zwitterionic MOFs.

## ■ ASSOCIATED CONTENT

### Supporting Information

The Supporting Information is available free of charge on the ACS Publications website at DOI: 10.1021/acs.chemmater.8b03885.

Details of ligand synthesis and characterization, PXRD patterns, TGA curves, NMR spectra, IR spectra, adsorption isotherms with Langmuir fits, and crystal structure packings (PDF)

cif file of **1′-Co** (CIF)

cif file of **1-Co** (CIF)

cif file of **1′-Ni** (CIF)

cif file of **1-Ni** (CIF)

cif file of **2-Co** (CIF)

cif file of **2-Ni** (CIF)

cif file of **3-Co** (CIF)

cif file of **4-Co** (CIF)

cif file of **4-Ni** (CIF)

cif file of **5-Ni** (CIF)

## ■ AUTHOR INFORMATION


### Corresponding Author

*Tel.: +1(315) 268-2355. Fax: +1(315) 268-6610. E-mail: mwriedt@clarkson.edu.

### ORCID

Timur Islamoglu: 0000-0003-3688-9158

Monu Joy: 0000-0003-1947-9691

Omar K. Farha: 0000-0002-9904-9845

Mario Wriedt: 0000-0003-3118-9507

### Author Contributions

§D.A. and T.I. contributed equally to this work.


### Notes

The authors declare no competing financial interest.

## ■ ACKNOWLEDGMENTS

M.W. gratefully acknowledges Clarkson University for generous start-up funding, the Donors of the American Chemical Society Petroleum Research Fund (Award No. 56295-DNI10), and the National Science Foundation CAREER Program (Award No. 1752771) for support of this research. Work carried out at the Advanced Light Source (ALS) was supported by the Director, Office of Science, Office of Basic Energy Science of the U.S. Department of Energy, under contract DE-AC02- 05CH11231. Work performed at the Advanced Photon Source at Argonne National Laboratory was supported by the U.S. Department of Energy, Office of Science, Office of Basic Energy Sciences, under Contract No. DE-AC02-06CH11357.

## ■ REFERENCES

(1) Li, J.-R.; Sculley, J.; Zhou, H.-C. Metal−Organic Frameworks for Separations. *Chem. Rev.* **2012**, *112*, 869−932.

(2) Bobbitt, N. S.; Mendonca, M. L.; Howarth, A. J.; Islamoglu, T.; Hupp, J. T.; Farha, O. K.; Snurr, R. Q. Metal−Organic Frameworks



DOI: 10.1021/acs.chemmater.8b03885
*Chem. Mater.* 2018, 30, 8332−8342

for the Removal of Toxic Industrial Chemicals and Chemical Warfare Agents. *Chem. Soc. Rev.* **2017**, *46*, 3357−3385.
(3) Denny, M. S., Jr; Moreton, J. C.; Benz, L.; Cohen, S. M. Metal−Organic Frameworks for Membrane-Based Separations. *Nat. Rev. Mater.* **2016**, *1*, 16078−16094.
(4) Bae, Y.-S.; Snurr, R. Q. Development and Evaluation of Porous Materials for Carbon Dioxide Separation and Capture. *Angew. Chem., Int. Ed.* **2011**, *50*, 11586−11596.
(5) Yang, R. T. *Adsorbents: Fundamentals and Applications*; John Wiley & Sons Inc.: Hoboken, 2003.
(6) He, Y.; Zhou, W.; Qian, G.; Chen, B. Methane Storage in Metal-Organic Frameworks. *Chem. Soc. Rev.* **2014**, *43*, 5657−78.
(7) Suh, M. P.; Park, H. J.; Prasad, T. K.; Lim, D.-W. Hydrogen Storage in Metal−Organic Frameworks. *Chem. Rev.* **2012**, *112*, 782−835.
(8) Hu, Z.; Deibert, B. J.; Li, J. Luminescent Metal-Organic Frameworks for Chemical Sensing and Explosive Detection. *Chem. Soc. Rev.* **2014**, *43*, 5815−5840.
(9) Aulakh, D.; Pyser, J. B.; Zhang, X.; Yakovenko, A. A.; Dunbar, K. R.; Wriedt, M. Metal−Organic Frameworks as Platforms for the Controlled Nanostructuring of Single-Molecule Magnets. *J. Am. Chem. Soc.* **2015**, *137*, 9254−9257.
(10) Aulakh, D.; Xie, H.; Shen, Z.; Harley, A.; Zhang, X.; Yakovenko, A. A.; Dunbar, K. R.; Wriedt, M. Systematic Investigation of Controlled Nanostructuring of Mn12 Single-Molecule Magnets Templated by Metal−Organic Frameworks. *Inorg. Chem.* **2017**, *56*, 6965−6972.
(11) Aulakh, D.; Bilan, H. K.; Wriedt, M. Porous Substrates as Platforms for the Nanostructuring of Molecular Magnets. *CrystEngComm* **2018**, *20*, 1011−1030.
(12) Zhu, L.; Liu, X.-Q.; Jiang, H.-L.; Sun, L.-B. Metal−Organic Frameworks for Heterogeneous Basic Catalysis. *Chem. Rev.* **2017**, *117*, 8129−8176.
(13) Huang, Y.-B.; Liang, J.; Wang, X.-S.; Cao, R. Multifunctional Metal−Organic Framework Catalysts: Synergistic Catalysis and Tandem Reactions. *Chem. Soc. Rev.* **2017**, *46*, 126−157.
(14) An, W.; Aulakh, D.; Zhang, X.; Verdegaal, W.; Dunbar, K. R.; Wriedt, M. Switching of Adsorption Properties in a Zwitterionic Metal−Organic Framework Triggered by Photogenerated Radical Triplets. *Chem. Mater.* **2016**, *28*, 7825−7832.
(15) Verdegaal, W. M.; Wang, K.; Sculley, J. P.; Wriedt, M.; Zhou, H.-C. Evaluation of Metal-Organic Frameworks and Porous Polymer Networks for CO2-Capture Applications. *ChemSusChem* **2016**, *9*, 636−643.
(16) Wriedt, M.; Sculley, J. P.; Verdegaal, W. M.; Yakovenko, A. A.; Zhou, H.-C. Unprecedented Activation and CO2 Capture Properties of an Elastic Single-Molecule Trap. *Chem. Commun.* **2013**, *49*, 9612−9614.
(17) Wriedt, M.; Sculley, J. P.; Yakovenko, A. A.; Ma, Y.; Halder, G. J.; Balbuena, P. B.; Zhou, H.-C. Low-Energy Selective Capture of Carbon Dioxide by a Pre-designed Elastic Single-Molecule Trap. *Angew. Chem., Int. Ed.* **2012**, *51*, 9804−9808.
(18) Islamoglu, T.; Goswami, S.; Li, Z.; Howarth, A. J.; Farha, O. K.; Hupp, J. T. Postsynthetic Tuning of Metal−Organic Frameworks for Targeted Applications. *Acc. Chem. Res.* **2017**, *50*, 805−813.
(19) Lu, W.; Wei, Z.; Gu, Z.-Y.; Liu, T.-F.; Park, J.; Park, J.; Tian, J.; Zhang, M.; Zhang, Q.; Gentle Iii, T.; Bosch, M.; Zhou, H.-C. Tuning the Structure and Function of Metal−Organic Frameworks via Linker Design. *Chem. Soc. Rev.* **2014**, *43*, 5561−5593.
(20) Destro, R.; Roversi, P.; Barzaghi, M.; Marsh, R. E. Experimental Charge Density of α-Glycine at 23 K. *J. Phys. Chem. A* **2000**, *104*, 1047−1054.
(21) Bae, Y. S.; Lee, C. H. Sorption Kinetics of Eight Gases on a Carbon Molecular Sieve at Elevated Pressure. *Carbon* **2005**, *43*, 95−107.
(22) Yang, N.-N.; Fang, J.-J.; Sui, Q.; Gao, E.-Q. Incorporating Electron-Deficient Bipyridinium Chromorphores to Make Multi-responsive Metal−Organic Frameworks. *ACS Appl. Mater. Interfaces* **2018**, *10*, 2735−2744.
(23) Yang, N.-N.; Sun, W.; Xi, F.-G.; Sui, Q.; Chen, L.-J.; Gao, E.-Q. Postsynthetic N-Methylation Making a Metal-Organic Framework Responsive to Alkylamines. *Chem. Commun.* **2017**, *53*, 1747−1750.
(24) Sui, Q.; Yang, N.-N.; Gong, T.; Li, P.; Yuan, Y.; Gao, E.-Q.; Wang, L. Impact of Lattice Water on Solid-State Electron Transfer in Viologen Pseudopolymorphs: Modulation of Photo- and Piezochromism. *J. Phys. Chem. Lett.* **2017**, *8*, 5450−5455.
(25) Sun, C.; Wang, M.-S.; Li, P.-X.; Guo, G.-C. Conductance Switch of a Bromoplumbate Bistable Semiconductor by Electron-Transfer Thermochromism. *Angew. Chem., Int. Ed.* **2017**, *56*, 554−558.
(26) Sui, Q.; Yuan, Y.; Yang, N.-N.; Li, X.; Gong, T.; Gao, E.-Q.; Wang, L. Coordination-Modulated Piezochromism in Metal-Viologen Materials. *J. Mater. Chem. C* **2017**, *5*, 12400−12408.
(27) Sui, Q.; Ren, X.-T.; Dai, Y.-X.; Wang, K.; Li, W.-T.; Gong, T.; Fang, J.-J.; Zou, B.; Gao, E.-Q.; Wang, L. Piezochromism and Hydrochromism through Electron Transfer: New Stories for Viologen Materials. *Chem. Sci.* **2017**, *8*, 2758−2768.
(28) Gong, T.; Yang, X.; Fang, J.-J.; Sui, Q.; Xi, F.-G.; Gao, E.-Q. Distinct Chromic and Magnetic Properties of Metal−Organic Frameworks with a Redox Ligand. *ACS Appl. Mater. Interfaces* **2017**, *9*, 5503−5512.
(29) Sun, J.-K.; Yang, X.-D.; Yang, G.-Y.; Zhang, J. Bipyridinium Derivative-Based Coordination Polymers: From Synthesis to Materials Applications. *Coord. Chem. Rev.* **2017**, DOI: 10.1016/j.ccr.2017.10.029.
(30) Sun, J.-K.; Zhang, J. Functional Metal−Bipyridinium Frameworks: Self-Assembly and Applications. *Dalton Trans.* **2015**, *44*, 19041−19055.
(31) Aulakh, D.; Varghese, J. R.; Wriedt, M. A New Design Strategy to Access Zwitterionic Metal−Organic Frameworks from Anionic Viologen Derivates. *Inorg. Chem.* **2015**, *54*, 1756−1764.
(32) Aulakh, D.; Nicoletta, A. P.; Varghese, J. R.; Wriedt, M. The Structural Diversity and Properties of Nine New Viologen Based Zwitterionic Metal-Organic Frameworks. *CrystEngComm* **2016**, *18*, 2189−2202.
(33) Toma, O.; Mercier, N.; Allain, M.; Kassiba, A. A.; Bellat, J.-P.; Weber, G.; Bezverkhyy, I. Photo- and Thermochromic and Adsorption Properties of Porous Coordination Polymers Based on Bipyridinium Carboxylate Ligands. *Inorg. Chem.* **2015**, *54*, 8923−8930.
(34) Higuchi, M.; Tanaka, D.; Horike, S.; Sakamoto, H.; Nakamura, K.; Takashima, Y.; Hijikata, Y.; Yanai, N.; Kim, J.; Kato, K.; Kubota, Y.; Takata, M.; Kitagawa, S. Porous Coordination Polymer with Pyridinium Cationic Surface, [Zn2(tpa)2(cpb)]. *J. Am. Chem. Soc.* **2009**, *131*, 10336−10337.
(35) *SAINT and APEX 2 Software for CCD Diffractometers*; Bruker AXS Inc.: Madison, WI, 2014.
(36) Sheldrick, G. M. *SADABS*, version 2014/4; University of Göttingen: Göttingen, Germany, 2014.
(37) Sheldrick, G. M. A short history of SHELX. *Acta Crystallogr., Sect. A: Found. Crystallogr.* **2008**, *64*, 112−122.
(38) Sheldrick, G. M. SHELXT-Integrated space-group and crystal-structure determination. *Acta Crystallogr., Sect. A: Found. Adv.* **2015**, *71*, 3−8.
(39) Sheldrick, G. M. Crystal structure refinement with SHELXL. *Acta Crystallogr., Sect. C: Struct. Chem.* **2015**, *71*, 3−8.
(40) Kissel, L.; Pratt, R. H. Corrections to Tabulated Anomalous-Scattering Factors. *Acta Crystallogr., Sect. A: Found. Crystallogr.* **1990**, *46*, 170−175.
(41) Farrugia, L. WinGX and ORTEP for Windows: An Update. *J. Appl. Crystallogr.* **2012**, *45*, 849−854.
(42) Macrae, C. F.; Bruno, I. J.; Chisholm, J. A.; Edgington, P. R.; McCabe, P.; Pidcock, E.; Rodriguez-Monge, L.; Taylor, R.; van de Streek, J.; Wood, P. A. Mercury CSD 2.0 - New Features for the Visualization and Investigation of Crystal Structures. *J. Appl. Crystallogr.* **2008**, *41*, 466−470.
(43) Zhang, Y. B.; Zhang, W. X.; Feng, F. Y.; Zhang, J. P.; Chen, X. M. A Highly Connected Porous Coordination Polymer with Unusual


DOI: 10.1021/acs.chemmater.8b03885
*Chem. Mater.* 2018, 30, 8332−8342

Channel Structure and Sorption Properties. *Angew. Chem., Int. Ed.* **2009**, *48*, 5287−5290.
(44) Jiang, G.; Wu, T.; Zheng, S.-T.; Zhao, X.; Lin, Q.; Bu, X.; Feng, P. A Nine-Connected Mixed-Ligand Nickel-Organic Framework and Its Gas Sorption Properties. *Cryst. Growth Des.* **2011**, *11*, 3713−3716.
(45) Zhang, Y.-B.; Zhou, H.-L.; Lin, R.-B.; Zhang, C.; Lin, J.-B.; Zhang, J.-P.; Chen, X.-M. Geometry Analysis and Systematic Synthesis of Highly Porous Isoreticular Frameworks with a Unique Topology. *Nat. Commun.* **2012**, *3*, 642−650.
(46) Zheng, S.-T.; Wu, T.; Chou, C.; Fuhr, A.; Feng, P.; Bu, X. Development of Composite Inorganic Building Blocks for MOFs. *J. Am. Chem. Soc.* **2012**, *134*, 4517−4520.
(47) Zhao, X.; Bu, X.; Wu, T.; Zheng, S.-T.; Wang, L.; Feng, P. Selective Anion Exchange with Nanogated Isoreticular Positive Metal-Organic Frameworks. *Nat. Commun.* **2013**, *4*, 2344−2352.
(48) Howarth, A. J.; Peters, A. W.; Vermeulen, N. A.; Wang, T. C.; Hupp, J. T.; Farha, O. K. Best Practices for the Synthesis, Activation, and Characterization of Metal−Organic Frameworks. *Chem. Mater.* **2017**, *29*, 26−39.
(49) Farha, O. K.; Hupp, J. T. Rational Design, Synthesis, Purification, and Activation of Metal−Organic Framework Materials. *Acc. Chem. Res.* **2010**, *43*, 1166−1175.
(50) Lin, J.-B.; Shimizu, G. K. H. Pyridinium Linkers and Mixed Anions in Cationic Metal−Organic Frameworks. *Inorg. Chem. Front.* **2014**, *1*, 302−305.
(51) Poloni, R.; Lee, K.; Berger, R. F.; Smit, B.; Neaton, J. B. Understanding Trends in CO2 Adsorption in Metal−Organic Frameworks with Open-Metal Sites. *J. Phys. Chem. Lett.* **2014**, *5*, 861−865.



DOI: 10.1021/acs.chemmater.8b03885
*Chem. Mater.* 2018, 30, 8332−8342